Low-Carbon Economic Operation of Power System Considering Regulation of Industrial Loads

Gengrui Chen[1], Hongxun Hui[1], Yi Ding[2], and Yonghua Song[1]

[1]University of Macau
[2]Zhejiang University

February 13, 2026

Low-Carbon Economic Operation of Power System Considering Regulation of Industrial Loads

Gengrui Chen, *Student Member, IEEE,* Hongxun Hui, *Senior Member, IEEE,* Yi Ding, *Member, IEEE,* Yonghua Song, *Fellow, IEEE*

***Abstract*—Industrial loads account for a large share of power consumption and possess significant regulation potential for achieving low-carbon economic operation in power systems. Among various industrial loads, the electric arc furnace (EAF) steel plant cluster is rapidly expanding and is characterized by large response capacity and strong price sensitivity. Consequently, it serves as an ideal flexible resource to participate in low-carbon demand response (LCDR). To this end, this paper proposes a source–load coordinated optimization method considering the regulation of EAF steel plant cluster. First, a continuous resource–task network is employed to establish an EAF steel plant cluster model, which captures the couplings among material, equipment, and energy across the production stages of EAF steelmaking. Second, a bidirectional dynamic decision-making–based source–load coordinated optimization method is developed, in which a Wasserstein-based distributionally robust optimization model and a nodal carbon intensity-based LCDR model are formulated for source-side and load-side, respectively. The two models are iteratively coordinated to achieve low-carbon economic operation of the system. Next, to overcome the challenge of computation time exceeding the unit time slot, a warm-start technique is developed to improve computational efficiency. Finally, numerical results on an improved IEEE 39-bus test system demonstrate the effectiveness of the proposed method.**

***Index Terms*—Low-carbon economic operation, low-carbon demand response, industrial load, distributionally robust optimization, source–load coordinated optimization.**

I. INTRODUCTION

A. Background and Literature Review

WITH the challenges of global energy transition and climate change, countries worldwide are accelerating adjustments in their energy structures to advance carbon neutrality [1]. The uncertainty of renewable energy, such as wind power and photovoltaic (PV), leads to power imbalance and increases operating costs [2]. Therefore, power system decarbonization requires larger support from flexible resources on the load side [3]. As a typical industrial load, electric arc furnace (EAF) steelmaking is recognized as a lower-carbon production process, as it enables higher renewable energy utilization [4]. In 2023, the global steel industry consumed approximately 1.39×10^9 MWh of electricity, and 29.1% of steel production was achieved through EAF steelmaking [5]. EAF steelmaking tends to be concentrated in industrial clusters within industrial zones [6]. It possesses significant advantages in response capacity and price sensitivity, making the EAF steel plant cluster an ideal flexible resource [7]. Accordingly, it is imperative to explore an operation strategy that mitigates renewable energy uncertainty and incentivizes the EAF steel plant cluster to support decarbonization, thereby achieving low-carbon economic operation of power systems.

Source–load coordinated optimization enables effective interaction between generation and load resources, facilitating joint decision-making, and serving as an effective approach to achieving economic operation of power systems [8]. Demand response (DR) is an important mechanism within source–load coordinated optimization to enhance the economic performance of power systems [9]. Although traditional DR can regulate loads through price-based incentive signals, it fails to fully exploit the carbon-reduction potential of load-side flexible resources [10]. Low-carbon demand response (LCDR) is a novel regulation mechanism in power systems designed to reduce carbon emissions [11]. It primarily uses the carbon price as an incentive signal to guide the load side in actively adjusting its power consumption behavior, thereby reducing system carbon emissions [12]. Zhang *et al.* [13] propose a low-carbon economic dispatch strategy for integrated energy systems under LCDR, considering the impact of energy storage on carbon emission flow. In [14], a novel information gap decision theory is developed to manage renewable energy uncertainty in energy stations considering LCDR, thereby achieving low-carbon economic operation. Although source–load coordinated optimization considering LCDR promotes power system decarbonization, existing studies pay insufficient attention to the carbon-reduction potential of industrial loads.

Leveraging the regulation potential of industrial loads can enhance renewable energy integration and provide a new pathway toward the low-carbon economic operation of power systems [15]. Foslie *et al.* [16] propose an industrial DR model that considers the joint production of chemical raw materials to reduce production costs and load demand during periods of high electricity prices. Bao *et al.* [17] propose an energy optimization strategy for flexible manufacturing industrial parks, considering complex production processes and improving PV utilization. Zhang *et al.* [18] propose a discrete industrial manufacturing scheduling framework that integrates energy, material, and carbon flow, considering the impact of production planning flexibility. The regulation of industrial loads in power systems should primarily focus on facilitating renewable energy integration. However, existing studies give insufficient attention to the impact of renewable energy uncertainty on the low-carbon economic operation of power systems.

To address the above issues, uncertainty optimization methods should be prioritized. Among them, distributionally robust optimization (DRO) is a data-driven optimization method that maintains robustness under uncertain environments [19]. It combines the advantages of stochastic programming (SP) and robust optimization (RO), enabling data-driven decisions without excessive conservatism [20]. Moreover, it can be deployed in two stages, where the computation of the offline preparation stage does not affect the operation stage. Several studies employ DRO to enable industrial loads to support the low-carbon economic operation of power systems. In [21], a two-stage DRO model is developed for coordinating steel plants and oxygen stations.

Gengrui Chen, Hongxun Hui, and Yonghua Song are with the State Key Laboratory of Internet of Things for Smart City, University of Macau, Macau 999078, China; Yi Ding is with the College of Electrical Engineering, Zhejiang University, Hangzhou 310027, China. (e-mail: gengrui.chen@connect.um.edu.mo).

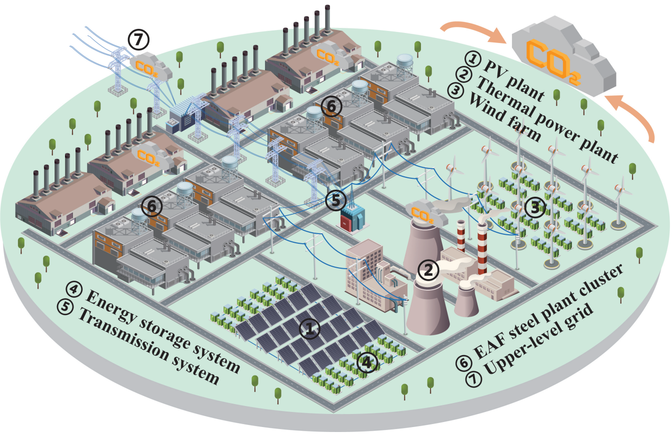

Fig. 1. Power system of the EAF steel plant cluster.

A data-driven ambiguity set is constructed to characterize demand uncertainty, resulting in more economical decision-making. Ning *et al*. [22] propose a data-driven multistage DRO framework for coupled electricity–hydrogen–refinery systems and develop an innovative Wasserstein-based ambiguity set. Case studies demonstrate that the proposed framework achieves a balance between economic efficiency and carbon reduction. Fu *et al.* [23] propose a distributionally robust chance-constrained model for multiple steel plants participating in the electricity market, incorporating conditional value-at-risk theory. Case studies demonstrate that the proposed method achieves a trade-off between risk and economic performance in energy management. However, studies on the regulation of EAF steel plant clusters in LCDR within power systems remain limited. Research on source–load coordinated optimization to promote joint decision-making of flexible resources on both sides is also insufficient. In addition, most methods for industrial loads participating in LCDR fail to consider the issue of computation time exceeding the unit time slot. Therefore, this study investigates a source–load coordinated optimization method considering the regulation of EAF steel plant cluster in LCDR to promote low-carbon economic operation of power systems.

B. Paper Structure and Contributions

The power system studied in this paper is illustrated in Fig. 1. It has power sources including thermal power plants, PV plants, wind farms, and energy storage systems, which jointly supply electricity to the EAF steel plant cluster in coordination with the upper-level grid. Building on the studies of resource–task network by Zhang *et al.* [24] and continuous resource–task network (cRTN) by Lyu *et al.* [25], this paper develops an EAF steel plant cluster model. Although system carbon emissions are primarily generated on the source side, load-side power consumption behavior significantly affects overall carbon reduction performance. Therefore, by allocating carbon emission responsibility to the load side, the total system cost is defined as the sum of operating cost and carbon emission cost. This paper adopts the nodal carbon intensity (NCI) theory [26] to quantify the carbon emissions transferred to the load side and to guide the participation of the EAF steel plant cluster in LCDR. In comparison with the existing studies, the contributions of this paper are summarized as follows:

1) A cRTN–based model of the EAF steel plant cluster is proposed. It considers the production stages of EAF steelmaking and captures the couplings among material, equipment, and energy to improve modeling accuracy. The proposed model leverages the computational efficiency of the cRTN to extend the single-plant model to a multi-plant cluster. This enables sufficient load-side flexibility resources to participate in LCDR and provides a feasible approach for industrial cluster dispatch.

2) A bidirectional dynamic decision-making–based source–load coordinated optimization method is developed, and its framework is shown in Fig. 2. To address renewable energy uncertainty and insufficient carbon-reduction incentive, a Wasserstein-based DRO model and a NCI-based LCDR model are proposed for source-side and load-side, respectively. The two models jointly mitigate the impact of renewable energy uncertainty and guide the cluster toward low-carbon power consumption. Through iterative coordination between the two models, the system achieves low-carbon economic operation.

3) A warm-start based source–load coordinated optimization algorithm is developed. A mapping function is constructed from the sample set to characterize the relationship between NCI and adjustment capability of the cluster. Based on this mapping, the algorithm generates the candidate initialization for iterative coordination between the two models in a data-driven manner. A feasible-set projection and proximal regularization are employed to refine candidate initialization and enhance convergence stability, thereby improving computational efficiency.

II. THE cRTN-BASED MODEL OF EAF STEEL PLANT CLUSTER

All steel plants analyzed in this paper adopt EAF steelmaking. The four production stages of EAF steelmaking are considered, and the process flow is shown in Fig. 3. First, the feedstock is melted into molten steel in the EAF. Next, molten steel is decarburized in the argon oxygen decarburization (AOD). Then, molten steel is refined in the ladle furnace (LF). Finally, slabs are produced in the continuous caster (CC).

A. Resource Balance Constraints

In this model, n, a, b, and t represent the bus, resource, task, and time slot indices, respectively. The variable $R_{n,a,t} \in [0,1]$ denotes the task progress of resource a at bus n during time slot t, where $R_{n,a,t} = 0$, $R_{n,a,t} \in (0,1)$, and $R_{n,a,t} = 1$ indicate no task, task in progress, and task completion, respectively. The design of $R_{n,a,t}$ provides a normalized representation of task progress, enabling a unified and solver-friendly formulation. To enable flexible task execution, a task state index $\theta \in \{0,1,2\}$ is introduced to represent the idle, minimum-speed, and maximum-speed states. The variable $s_{n,a,b,\theta} \in \mathbb{R}$ denotes the task processing rate, defined as the amount of resource a produced or consumed by task b in state θ.

$$\begin{aligned} & R_{n,a,t} \leq R_{n,a,t-1} + \sum_{b} \sum_{\theta} s_{n,a,b,\theta} D_{n,b,\theta,t}, \\ & \forall n \in \Omega_{\mathrm{ST}},\ \forall a \in \Omega_{\mathrm{RE}},\ \forall b \in \Omega_{\mathrm{TA}},\ \forall t \end{aligned} \tag{1}$$

where $D_{n,b,\theta,t}$ is a continuous variable denoting the processing time; Ω_{TA}, Ω_{RE}, and Ω_{ST} denote the sets of tasks, resources, and steel plant buses, respectively.

B. Task Execution Time Constraints

To enable flexible scheduling under varying processing rates $s_{n,a,b,\theta}$, task execution time constraints are formulated to regulate task processing time and state transition within a unit

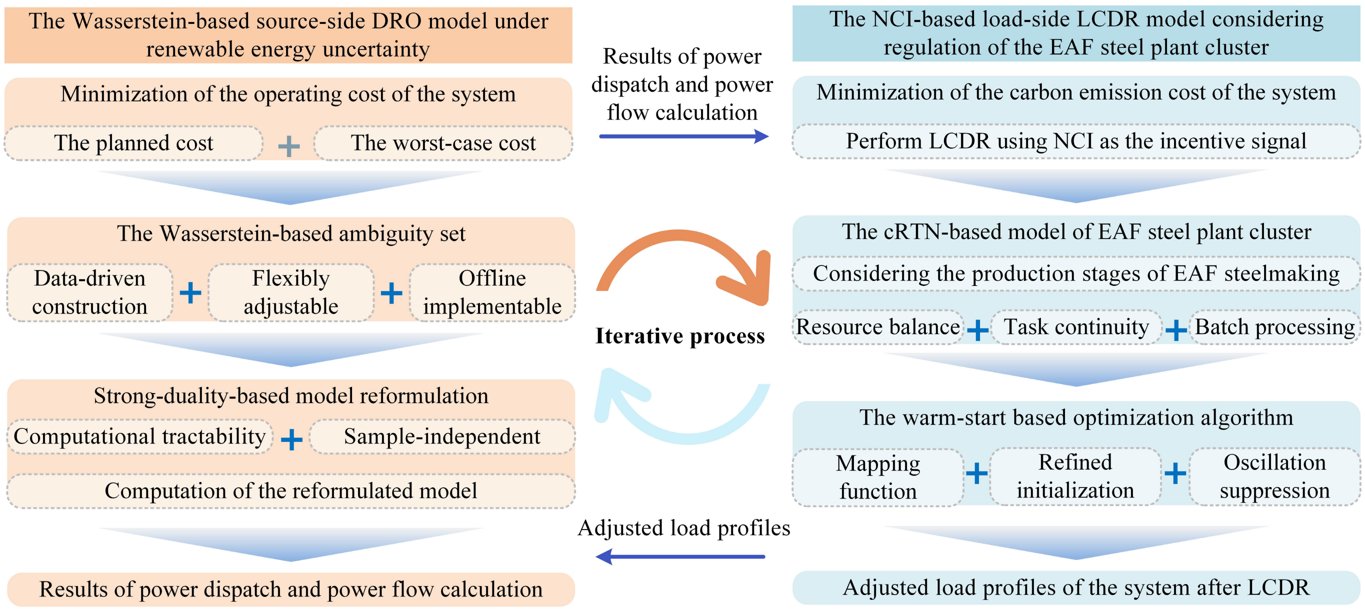

Fig. 2. Bidirectional dynamic decision-making–based source–load coordinated optimization framework.

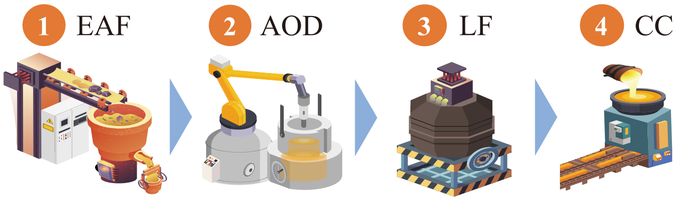

Fig. 3. The four production stages of the EAF steelmaking [27].

time slot τ. Eq. (2) ensures that the processing time in each state does not exceed τ. Eq. (3) ensures that the total processing time across all states equals τ.

$$0 \leq D_{n,b,\theta,t} \leq \tau, \ \forall n \in \Omega_{\mathrm{ST}}, \ \forall b \in \Omega_{\mathrm{TA}}, \ \forall t \tag{2}$$

$$\sum_{\theta} D_{n,b,\theta,t} = \tau, \ \forall n \in \Omega_{\mathrm{ST}}, \ \forall b \in \Omega_{\mathrm{TA}}, \ \forall t \tag{3}$$

C. Task Continuity Constraints

Some resource-producing tasks $R_{a^{b+},t}$ are uninterruptible once initiated and are therefore prevented from entering the idle state $D_{n,b,0,t}$. Accordingly, (4) and (5) are introduced to ensure task continuity during execution.

$$D_{n,b,0,t} \leq 1 - \varepsilon_{n,b,t}, \ \forall n \in \Omega_{\mathrm{ST}}, \ \forall b \in \Omega_{\mathrm{TA}}, \ \forall t \tag{4}$$

$$R_{a^{b+},t} \leq \varepsilon_{n,b,t}, \ \forall n \in \Omega_{\mathrm{ST}}, \ \forall b \in \Omega_{\mathrm{TA}}, \ \forall t \tag{5}$$

where $\varepsilon_{n,b,t}$ is a binary variable; a^{b-} and a^{b+} denote indices of resource a consumed and produced by task b, respectively.

D. Waiting Task Constraints

Waiting tasks represent the dwell of resources between two production stages. The dwell time consists of the transfer time $\hat{T}^{1}_{n,b}$ and the maximum waiting time $\hat{T}^{2}_{n,b}$. Hence, (6) defines the minimum and maximum processing rates of waiting tasks as $s^{\mathrm{W}}_{n,a,b,1}$ and $s^{\mathrm{W}}_{n,a,b,2}$, corresponding to $\theta = 1$ and 2, respectively.

$$\begin{cases} s^{\mathrm{W}}_{n,a,b,1} = 1/\left(\hat{T}^{1}_{n,b} + \hat{T}^{2}_{n,b}\right) \\ s^{\mathrm{W}}_{n,a,b,2} = 1/\left(\hat{T}^{1}_{n,b}\right) \end{cases} \tag{6}$$

$$R_{a^{b-},t} \leq \varepsilon_{n,b,t}, \ \forall n \in \Omega_{\mathrm{ST}}, \ \forall b \in \Omega_{\mathrm{TA}}, \ \forall t \tag{7}$$

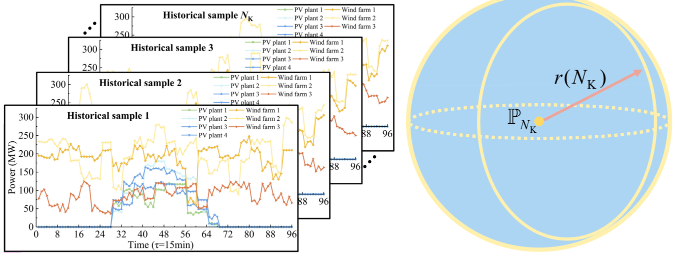

(a) (b)

Fig. 4. Construction of ambiguity set: (a) sample set; (b) Wasserstein ball.

Eqs. (4) and (7) indicate that resource-consuming tasks $R_{a^{b-},t}$ are executed immediately after the completion of waiting tasks and are therefore prevented from entering the idle state $D_{n,b,0,t}$.

E. Batch Processing Logic Constraints

Steel production exhibits a batch-based execution pattern. For instance, each batch of feedstock must complete the melting process before the subsequent task begins. Together with the task continuity constraints, (8) establishes a complete modeling framework, ensuring that each task is completed ($R_{n,a,t} = 1$) after an integer number of time slots.

$$\begin{cases} D_{n,b,1,t} = \varepsilon_{n,b,t} \cdot \tau \\ s_{n,a^{b+},b,1} = 1/\left(\left\lceil \hat{T}_{n,b}/\tau \right\rceil \cdot \tau\right) \\ s_{n,a^{b-},b,1} = -1/\left(\left\lceil \hat{T}_{n,b}/\tau \right\rceil \cdot \tau\right) \end{cases} \tag{8}$$
$$\forall n \in \Omega_{\mathrm{ST}}, \ \forall b \in \Omega_{\mathrm{TA}}, \ \forall t$$

where $\hat{T}_{n,b}$ denotes the processing time of task b at bus n; $\lceil \cdot \rceil$ represents the ceiling operator, which ensures that the processing time is fully covered by an integer number of time slots.

III. THE WASSERSTEIN-BASED SOURCE-SIDE DRO MODEL UNDER RENEWABLE ENERGY UNCERTAINTY

A. Wasserstein-based Ambiguity Set

The ambiguity set plays a central role in DRO, as it characterizes the uncertainty in the probability distribution of the random variable. The ambiguity set is constructed using the Wasserstein metric, which is particularly suitable for scenarios supported by historical data. Given a historical sample $\hat{\boldsymbol{u}}_h$ in historical sample set $\left\{\hat{\boldsymbol{u}}_1, \hat{\boldsymbol{u}}_2, \ldots, \hat{\boldsymbol{u}}_{N_{\mathrm{K}}}\right\}$ with sample size N_{K}, as shown in Fig. 4(a), the empirical distribution $\mathbb{P}_{N_{\mathrm{K}}}$ can be constructed as in (9), which serves as a surrogate for the unknown true distribution $\mathbb{P}$ of random variable $\tilde{\boldsymbol{u}}$. The Wasserstein metric $W(\mathbb{P}_{N_{\mathrm{K}}}, \mathbb{P})$, which measures the distance between $\mathbb{P}_{N_{\mathrm{K}}}$ and $\mathbb{P}$, is defined in (10).

$$\mathbb{P}_{N_{\mathrm{K}}} = \frac{1}{N_{\mathrm{K}}} \sum_{h=1} \delta_{\hat{\boldsymbol{u}}_h} \tag{9}$$

$$W(\mathbb{P}_{N_{\mathrm{K}}}, \mathbb{P}) = \inf_{\Pi \in \Gamma(\mathbb{P}_{N_{\mathrm{K}}}, \mathbb{P})} \left\{ \int_{\Xi^2} \|\hat{\boldsymbol{u}} - \tilde{\boldsymbol{u}}\| \, \Pi(d\hat{\boldsymbol{u}}, d\tilde{\boldsymbol{u}}) \right\} \tag{10}$$

where $\delta_{\hat{\boldsymbol{u}}_h}$ denotes the Dirac measure centered at $\hat{\boldsymbol{u}}_h$; $\Gamma(\mathbb{P}_{N_{\mathrm{K}}}, \mathbb{P})$ represents the set of all joint distributions with marginals $\mathbb{P}_{N_{\mathrm{K}}}$ and $\mathbb{P}$; Ξ^2 denotes the Cartesian product of the support set Ξ with itself, representing the domain of the joint distribution Π.

Hence, $\mathbb{P}$ lies within the Wasserstein-based ambiguity set defined in (11), where $\hat{\mathcal{P}}_{N_{\mathrm{K}}}$ denotes the Wasserstein ball of radius $r(N_{\mathrm{K}})$ centered at $\mathbb{P}_{N_{\mathrm{K}}}$, as illustrated in Fig. 4(b). Since $r(N_{\mathrm{K}})$ plays a critical role in determining the effectiveness of the DRO model, it is calculated based on (12) and (13) in [28].

$$\hat{\mathcal{P}}_{N_{\mathrm{K}}} = \left\{\mathbb{P} \in \mathcal{P}(\Xi) : W(\mathbb{P}_{N_{\mathrm{K}}}, \mathbb{P}) \le r(N_{\mathrm{K}})\right\} \tag{11}$$

$$r(N_{\mathrm{K}}) = D_{N_{\mathrm{K}}} \sqrt{\frac{1}{N_{\mathrm{K}}} \log\left(\frac{1}{1-\lambda}\right)} \tag{12}$$

$$D_{N_{\mathrm{K}}} \approx 2 \inf_{\varphi > 0} \sqrt{\frac{1}{2\varphi}\left(1 + \ln\left(\frac{1}{N_{\mathrm{K}}} \sum_{h=1} e^{\varphi \|\hat{\boldsymbol{u}}_h - \hat{\boldsymbol{\mu}}\|_1^2}\right)\right)} \tag{13}$$

where $\mathcal{P}(\Xi)$ denotes the set of all probability distributions supported on Ξ, and λ represents the confidence level; $\hat{\boldsymbol{\mu}}$ denotes the sample mean, and $|\cdot|_1^2$ represents the squared ℓ_1-norm; $D_{N_{\mathrm{K}}}$ is associated with the positive relaxation parameter φ.

B. Objective Function of Source-side DRO Model

Eq. (14) represents the minimization of the operating cost of the system, where f_1 and f_2 denote the planned cost and the worst-case cost, respectively. The uncertainty is defined as a random variable $\tilde{\psi}_t$ in (17) for computational tractability, representing the total renewable energy deviation of the system.

$$f_{\mathrm{OPE}} = \min[f_1 + \sup_{\mathbb{P} \in \hat{\mathcal{P}}_{N_{\mathrm{K}}}} \mathbb{E}_{\mathbb{P}}(f_2)] \tag{14}$$

$$\begin{aligned} f_1 = & \sum_{t=1} \sum_{i=1} \left(C_i^{\mathrm{R}} \alpha_{i,t} + C_i^{\mathrm{ON}} \beta_{i,t} + C_i^{\mathrm{OFF}} \gamma_{i,t} + C_i^{\mathrm{MT}} \omega_{i,t} + \tau C_i^{\mathrm{G}} P_{i,t}^{\mathrm{G}}\right) \\ & + \tau \sum_{t=1} \sum_{m=1} C_t^{\mathrm{ES}} \left(P_{m,t}^{\mathrm{CHR}} - P_{m,t}^{\mathrm{DIS}}\right) + \tau \sum_{t=1} \sum_{q=1} C_t^{\mathrm{UP}} \left(P_{q,t}^{\mathrm{IN}} - P_{q,t}^{\mathrm{OUT}}\right) \end{aligned} \tag{15}$$

$$f_2 = \tau \sum_{t=1} \left[U_t^{\mathrm{DE}} \times (\tilde{\psi}_t)^-\right] + \tau \sum_{t=1} \left[U_t^{\mathrm{EN}} \times (\tilde{\psi}_t)^+\right] \tag{16}$$

$$\tilde{\psi}_t = \sum_{k=1} \left(\tilde{P}_{k,t}^{\mathrm{PV}} - P_{k,t}^{\mathrm{PV}}\right) + \sum_{w=1} \left(\tilde{P}_{w,t}^{\mathrm{W}} - P_{w,t}^{\mathrm{W}}\right) \tag{17}$$

$$U_t^{\mathrm{DE}} = \sum_{i=1} U_i^{\mathrm{G}} \nu_{i,t}^{\mathrm{G}} + \sum_{m=1} U_m^{\mathrm{ES}} \nu_{m,t}^{\mathrm{ES}} + \sum_{q=1} U_q^{\mathrm{UP}} \nu_{q,t}^{\mathrm{UP}} \tag{18}$$

$$\sum_{i=1} \nu_{i,t}^{\mathrm{G}} + \sum_{m=1} \nu_{m,t}^{\mathrm{ES}} + \sum_{q=1} \nu_{q,t}^{\mathrm{UP}} = 1, \ \forall t \tag{19}$$

where $\alpha_{i,t}$, $\beta_{i,t}$, $\gamma_{i,t}$, and $\omega_{i,t}$ denote the binary state variables representing the online, startup, shutdown, and maintenance states of thermal power plants, respectively; $P_{i,t}^{\mathrm{G}}$, $P_{m,t}^{\mathrm{CHR}}$, $P_{m,t}^{\mathrm{DIS}}$, P_t^{IN}, and P_t^{OUT} denote the real-valued decision variables representing the power output of thermal power plants, the charging and discharging power of energy storage systems, and the power exchanged with the upper-level grid, respectively; $P_{k,t}^{\mathrm{PV}}$ and $P_{w,t}^{\mathrm{W}}$ denote the real-valued decision variables representing the expected power of the PV plant and wind farm to be utilized by the system, respectively; $\tilde{P}_{k,t}^{\mathrm{PV}}$ and $\tilde{P}_{w,t}^{\mathrm{W}}$ denote the random variables representing the actual available power of the PV plant and wind farm, respectively; $\nu_{i,t}^{\mathrm{G}}$, $\nu_{m,t}^{\mathrm{ES}}$, and $\nu_{q,t}^{\mathrm{UP}} \in [0,1]$ denote the participation factors associated with each component; $f_{\mathrm{CUT}} = \sum_{t=1} \left[U^{\mathrm{EN}} \times (\tilde{\psi}_t)^+\right]$ denotes the cost of renewable energy curtailment; C denotes the cost coefficients associated with each component; U denotes the penalty cost coefficients for deviations in renewable generation output of each component; $(x)^+$ and $(x)^-$ represent $\max(x, 0)$ and $\max(-x, 0)$, respectively.

Eq. (16) is computationally intractable and can be transformed into (20) via strong duality theory. However, the constraints in (20) scale with the sample size, imposing a heavy computational burden that limits the effective utilization of historical data. To address this issue, the method proposed in [29] is adopted to reformulate (20) into a tractable approximation. Given the structure of f_2, there exists a family of affine functions of $\tilde{\psi}_t$, expressed as $c_M \tilde{\psi}_t + d_M$, such that (21) holds.

$$\begin{aligned} & \sup_{\mathbb{P} \in \widehat{\mathcal{P}}_{N_{\mathrm{K}}}} \mathbb{E}_{\mathbb{P}}[f_2(\tilde{\psi}_t)] \\ & = \inf_{\kappa_t \ge 0} \left\{ \kappa_t \cdot r_t + \tfrac{1}{N_{\mathrm{K}}} \sum_{h=1}^{N_{\mathrm{K}}} \sup_{\tilde{\psi}_t \in \Xi} \left[f_2(\tilde{\psi}_t) - \kappa_t \cdot \left\|\tilde{\psi}_t - \hat{\psi}_{t,h}\right\|_1\right] \right\} \\ & = \begin{cases} \inf\limits_{\kappa_t \ge 0} & \kappa_t \cdot r_t + \tfrac{1}{N_{\mathrm{K}}} \sum_{h=1}^{N_{\mathrm{K}}} \varsigma_{t,h} \\ \text{s.t.} & f_2(\overline{\psi}_t) - \kappa_t \cdot \left(\overline{\psi}_t - \hat{\psi}_{t,h}\right) \le \varsigma_{t,h}, \ \forall h \le N_{\mathrm{K}} \\ & f_2(\underline{\psi}_t) + \kappa_t \cdot \left(\underline{\psi}_t - \hat{\psi}_{t,h}\right) \le \varsigma_{t,h}, \ \forall h \le N_{\mathrm{K}} \\ & f_2(\hat{\psi}_{t,h}) \le \varsigma_{t,h}, \ \forall h \le N_{\mathrm{K}} \end{cases} \end{aligned} \tag{20}$$

$$f_2(\tilde{\psi}_t) = \max_{M \in \{1,2\}} \left\{c_M \tilde{\psi}_t + d_M\right\} = \begin{cases} \sum_{t=1} U_t^{\mathrm{EN}} \tilde{\psi}_t, \tilde{\psi}_t \ge 0 \\ -\sum_{t=1} U_t^{\mathrm{DE}} \tilde{\psi}_t, \tilde{\psi}_t < 0 \end{cases} \tag{21}$$

where κ_t and $\varsigma_{t,h}$ denote the dual variable and the auxiliary variable, respectively; $\overline{\psi}_t$ and $\underline{\psi}_t$ denote the upper and lower boundaries of the support set, respectively; c_M and d_M represent the coefficient and the intercept of the affine functions.

Hence, (20) is reformulated into a sample-independent form.

$$\begin{aligned} & \sup_{\mathbb{P} \in \widehat{\mathcal{P}}_{N_{\mathrm{K}}}} \mathbb{E}_{\mathbb{P}}[f_2(\tilde{\psi}_t)] \\ & = \begin{cases} \inf\limits_{\kappa_t \ge 0} & \left\{ \begin{aligned} & \kappa_t \cdot r_t + \chi \cdot \overline{\psi}_t - \upsilon \cdot \underline{\psi}_t \\ & + \tfrac{1}{N_{\mathrm{K}}} \sum_{h=1}^{N_{\mathrm{K}}} \left[f_2(\hat{\psi}_{t,h}) + (\chi - \upsilon)\, \hat{\psi}_{t,h}\right] \end{aligned} \right\} \\ \text{s.t.} & \|\chi - \upsilon - c_M\|_\infty \le \kappa_t, \ \forall M \in \{1,2\} \\ & \chi, \upsilon \ge 0 \end{cases} \end{aligned} \tag{22}$$

where χ and υ denote Lagrange multipliers; $\|\cdot\|_\infty$ is ℓ_∞-norm.

C. Constraints of Source-side DRO Model

Eqs. (23)–(25) specify the state constraints of thermal power plant; (26)–(31) represent the limiting constraints; (32)-(33) correspond to the ramping constraints; (34)-(35) define the power flow security and power balance constraints, respectively.

$$\beta_{i,t} + \gamma_{i,t} \le 1, \ \forall i, t \tag{23}$$

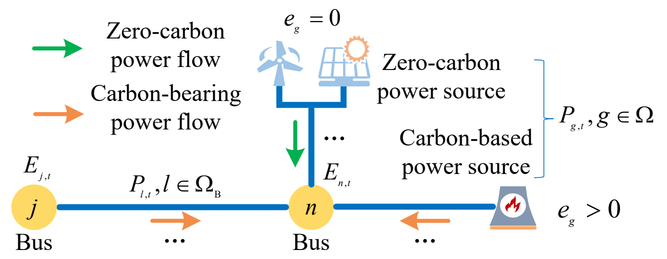

Fig. 5. Schematic diagram of the NCI components at bus n.

$$\alpha_{i,t} + \omega_{i,t} \le 1,\ \forall i,t \tag{24}$$

$$\begin{cases} \beta_{i,t} - \gamma_{i,t} = \alpha_{i,t}, & t=1,\ \forall i \\ \beta_{i,t} - \gamma_{i,t} = \alpha_{i,t} - \alpha_{i,t-1}, & t \ge 2,\ \forall i \end{cases} \tag{25}$$

$$0 \le P_{q,t}^{\mathrm{IN}} \le \sigma_{q,t}^{\mathrm{UP}} P_{q,t}^{\mathrm{INmax}},\ \forall q,t \tag{26}$$

$$0 \le P_{q,t}^{\mathrm{OUT}} \le (1-\sigma_{q,t}^{\mathrm{UP}}) P_{q,t}^{\mathrm{OUTmax}},\ \forall q,t \tag{27}$$

$$\alpha_{i,t} P_{i,t}^{\mathrm{G\,min}} \le P_{i,t}^{\mathrm{G}} \le \alpha_{i,t} P_{i,t}^{\mathrm{G\,max}},\ \forall i,t \tag{28}$$

$$0 \le P_{m,t}^{\mathrm{DIS}} \le \sigma_{m,t}^{\mathrm{ES}} R_m^{\mathrm{ES}} W_m^{\mathrm{ES}},\ \forall m,t \tag{29}$$

$$0 \le P_{m,t}^{\mathrm{CHR}} \le (1-\sigma_{m,t}^{\mathrm{ES}}) R_m^{\mathrm{ES}} W_m^{\mathrm{ES}},\ \forall m,t \tag{30}$$

$$\begin{cases} 0 \le Q_{m,t+1} \le W_m^{\mathrm{ES}}, Q_{m,1} = Q_{m,T+1},\ \forall m,t \\ Q_{m,t+1} = Q_{m,t} + \tau[\eta_{\mathrm{ES}} P_{m,t+1}^{\mathrm{CHR}} - (1/\eta_{\mathrm{ES}}) P_{m,t+1}^{\mathrm{DIS}}] \end{cases} \tag{31}$$

$$P_{i,t}^{\mathrm{G}} - P_{i,t-1}^{\mathrm{G}} < (1-\alpha_{i,t-1}) P_{i,t}^{\mathrm{G\,max}} + \alpha_{i,t-1} D^{\mathrm{UR}},\ t \ge 2,\ \forall i \tag{32}$$

$$P_{i,t-1}^{\mathrm{G}} - P_{i,t}^{\mathrm{G}} < (1-\alpha_{i,t}) P_{i,t}^{\mathrm{G\,max}} + \alpha_{i,t} D^{\mathrm{UR}},\ t \ge 2,\ \forall i \tag{33}$$

$$\begin{aligned} -P_l^{\max} \le P_{l,t} &= \sum_{i=1} G_{l-i} P_{i,t}^{\mathrm{G}} + \sum_{k=1} G_{l-k} P_{k,t}^{\mathrm{PV}} \\ &+ \sum_{w=1} G_{l-w} P_{w,t}^{\mathrm{W}} + \sum_{q=1} G_{l-q}^{\mathrm{UP}} (P_{q,t}^{\mathrm{IN}} - P_{q,t}^{\mathrm{OUT}}) \\ &- \sum_{n=1} G_{l-n} P_{n,t}^{\mathrm{L}} + \sum_{m=1} G_{l-m} (P_{m,t}^{\mathrm{DIS}} - P_{m,t}^{\mathrm{CHR}}) \le P_l^{\max} \end{aligned} \tag{34}$$

$$\begin{aligned} &\sum_{i=1} P_{i,t}^{\mathrm{G}} + \sum_{k=1} P_{k,t}^{\mathrm{PV}} + \sum_{w=1} P_{w,t}^{\mathrm{W}} + \sum_{m=1} (P_{m,t}^{\mathrm{DIS}} - P_{m,t}^{\mathrm{CHR}}) \\ &+ \sum_{q=1} (P_{q,t}^{\mathrm{IN}} - P_{q,t}^{\mathrm{OUT}}) = \sum_{n=1} P_{n,t}^{\mathrm{L}} \end{aligned} \tag{35}$$

where G denotes the power transfer distribution factor; $P_{l,t}$, $P_l^{\max}$, and $P_{n,t}^{\mathrm{L}}$ signify the power flow, the transmission capacity, and the load demand, respectively; $\sigma_{q,t}^{\mathrm{UP}}$ and $\sigma_{m,t}^{\mathrm{ES}}$ signify the binary state variables of the upper-level grid and energy storage, respectively; $Q_{m,t}$, R_m^{ES}, W_m^{ES}, and η_{ES} denote the stored energy, the power-to-energy ratio, the energy storage capacity, and efficiency, respectively; $P_{i,t}^{\mathrm{G\,min}}$, $P_{i,t}^{\mathrm{G\,max}}$, $P_{q,t}^{\mathrm{OUTmax}}$, and $P_{q,t}^{\mathrm{INmax}}$ signify the power limits; D^{UR} denotes the ramping coefficient.

IV. THE NCI-BASED LOAD-SIDE LCDR MODEL CONSIDERING REGULATION OF EAF STEEL PLANT CLUSTER

A. NCI-Based Load-Side LCDR Optimization Model

The NCI, expressed in kgCO$_2$/MWh and defined in (36), dynamically quantifies the carbon emissions that result from the consumption of a unit of electrical energy. The schematic diagram of the NCI components at bus n is shown in Fig. 5. The power sources of the system are classified into carbon-based and zero-carbon types. The former, including thermal power plants and the upper-level grid, emit carbon, whereas the latter, including PV plants and wind farms, are emission-free.

$$E_{n,t} = \frac{\sum\limits_{l \in \Omega_{\mathrm{B}}} P_{l,t} E_{j,t} + \sum\limits_{g \in \Omega} P_{g,t} e_g}{\sum\limits_{l \in \Omega_{\mathrm{B}}} P_{l,t} + \sum\limits_{g \in \Omega} P_{g,t}},\ \forall n,t \tag{36}$$

where $E_{n,t}$ and $E_{j,t}$ denote the NCI of buses n and j, respectively; $P_{g,t}$ and e_g indicate the output and the carbon intensity of each power source, respectively; Ω_{B} denotes the set of all transmission lines injecting active power into bus n, and Ω denotes the set of all power sources connected to bus n.

Therefore, the EAF steel plant cluster participates in LCDR according to $E_{n,t}$. The objective function of the LCDR optimization model, given in (37), aims to minimize the carbon emission cost of the system. Eq. (38) defines $EN_{n,t}$ as the energy consumption of bus n.

$$f_{\mathrm{CO2}} = \min C^{\mathrm{C}} \sum_{n=1} \sum_{t=1} \left(E_{n,t} \cdot EN_{n,t}\right) \tag{37}$$

$$EN_{n,t} = P_{n,t}^{\mathrm{L}} \cdot \tau = \begin{cases} \sum\limits_{b} \sum\limits_{\theta} P_{n,b,\theta} \cdot D_{n,b,\theta,t}, & \text{if } n \in \Omega_{\mathrm{ST}} \\ P_{n,t}^{\mathrm{OT}} \cdot \tau, & \text{otherwise} \end{cases} \tag{38}$$

where C^{C}, $P_{n,b,\theta}$, and $P_{n,t}^{\mathrm{OT}}$ denote the carbon cost coefficient, the EAF steel plant load, and other load, respectively.

Eqs. (39)-(41) specify the energy consumption variation $\Delta EN_{n,t}$ for each iteration and its upper and lower bounds. Eq. (42) ensures that the total energy consumption remains constant over the time horizon T.

$$\Delta EN_{n,t} = EN_{n,t} - EN_{n,t}^{(0)} = \begin{cases} EN_{n,t}^{\mathrm{U}}, & \Delta EN_{n,t} \ge 0 \\ EN_{n,t}^{\mathrm{D}}, & \Delta EN_{n,t} < 0 \end{cases} \tag{39}$$

$$0 \le EN_{n,t}^{\mathrm{U}} \le I_{n,t} \cdot \rho_{n,t}^{\max} \cdot EN_{n,t}^{(0)},\ \forall n,t \tag{40}$$

$$-(1-I_{n,t}) \cdot \rho_{n,t}^{\max} \cdot EN_{n,t}^{(0)} \le EN_{n,t}^{\mathrm{D}} \le 0,\ \forall n,t \tag{41}$$

$$\sum_{t=1} EN_{n,t}^{\mathrm{U}} = \sum_{t=1} \left|EN_{n,t}^{\mathrm{D}}\right|,\ \forall n,t \tag{42}$$

where $EN_{n,t}^{(0)}$, $EN_{n,t}^{\mathrm{U}}$, and $EN_{n,t}^{\mathrm{D}}$ denote the initial energy consumption, the upward and downward adjustment amounts, respectively; $I_{n,t}$ denotes the binary state variable; $\rho_{n,t}^{\max}$ denotes the expected energy consumption adjustment rate (EECR), representing the upper limit of the adjustment capability of the EAF steel plant cluster participating in LCDR.

B. Warm-Start Technology

In the proposed method, the source-side and load-side models require multiple iterations to reach convergence. This process may result in computation time exceeding τ, which is undesirable for power system operation and steel production scheduling. To overcome this issue, a warm-start–based source–load coordinated optimization algorithm is developed.

By rearranging (39)–(41), (43) is obtained, based on which energy consumption adjustment rate (ECR) is defined in (44).

$$-\rho_{n,t}^{\max} \le \frac{\Delta EN_{n,t}^{(z)}}{EN_{n,t}^{(z-1)}} \le \rho_{n,t}^{\max}, \quad z \ge 1,\ \forall n,t \tag{43}$$

$$\rho_{n,t}^{(z)} = \frac{\Delta EN_{n,t}^{(z)}}{EN_{n,t}^{(z-1)}} \times 100\%, \quad z \ge 1,\ \forall n,t \tag{44}$$

where $\rho_{n,t}^{(z)}$ is the ECR in the z-th iteration; z is iteration index.

Since $EN_{n,t}^{(z-1)}$ is constant in the z-th iteration, $f_{\mathrm{CO2}}^{(z)}$ is regarded as a function of $E_{n,t}^{(z)}$ and $\rho_{n,t}^{(z)}$. Accordingly, $f_{\mathrm{CO2}}^{(z)}$ in the z-th iteration can be expressed as (45):

$$\begin{cases} f_{\mathrm{CO2}}^{(z)} = \min C^{\mathrm{C}} \sum\limits_{n=1} \sum\limits_{t=1} \left[E_{n,t}^{(z)} \cdot EN_{n,t}^{(z)}\right] \\ EN_{n,t}^{(z)} = EN_{n,t}^{(z-1)} \left(1 + \rho_{n,t}^{(z)}\right), \quad z \ge 1 \end{cases} \tag{45}$$

Algorithm 1 Warm-Start Based Source–Load Coordinated Optimization Algorithm

Step 1. Initialize iteration index as $z = 1$ and energy consumption data as $EN_{n,t}^{(0)}$. Specify the convergence tolerance $\epsilon > 0$ and the proximal coefficient $\xi > 0$. For clarity of presentation, all algorithmic formulas are expressed in matrix form.

Step 2. Using the results at $z = 1$ as the sample data, a monotone Lipschitz fitting method is employed to construct a mapping function $\tilde{f}_n$ for each bus n, which preliminarily characterizes the relationship between $\boldsymbol{E}_n$ and $\boldsymbol{\rho}_n$:

$$\boldsymbol{\rho}_n = \tilde{f}_n(\boldsymbol{E}_n), \quad \tilde{f}_n : \mathbb{R}^T \to \mathbb{R}^T \tag{46}$$

The matrix-form operator $F(\cdot)$ is obtained by stacking the mappings across all buses and time slots, as shown in (47):

$$\boldsymbol{\rho} = F(\boldsymbol{E}), \quad F : \mathbb{R}^{N\times T} \to \mathbb{R}^{N\times T} \tag{47}$$

Step 3. For computational tractability and to avoid excessive computational burden, hard constraints are extracted from (1)–(8) and (39)–(42) to construct a convex inner approximation feasible set S:

$$S = \{\boldsymbol{\rho} : \boldsymbol{A}\boldsymbol{\rho} \leq \boldsymbol{c},\ \boldsymbol{H}\boldsymbol{\rho} = \boldsymbol{d}\} \subseteq \mathcal{F} \tag{48}$$

where $\mathcal{F}$ denotes the complete feasible region defined by (1)–(8), while $\boldsymbol{A}$, $\boldsymbol{H}$, $\boldsymbol{c}$, and $\boldsymbol{d}$ are constant matrices.

Step 4. For $z \geq 2$, the source-side DRO model is solved based on $EN_{n,t}^{(z-1)}$ and $\boldsymbol{E}^{(z)}$ is computed according to (36). The result is then fed into $F(\cdot)$ to obtain the candidate initialization $\hat{\boldsymbol{\rho}}^{(z)}$:

$$\hat{\boldsymbol{\rho}}^{(z)} = F\left(\boldsymbol{E}^{(z)}\right) \tag{49}$$

However, $\hat{\boldsymbol{\rho}}^{(z)}$ obtained from (37) may deviate from constraints of steel production. To further provide a feasible and reliable initialization for iteration, the projection of $\hat{\boldsymbol{\rho}}^{(z)}$ onto S is computed according to (50), yielding refined initialization $\tilde{\boldsymbol{\rho}}^{(z)}$.

$$\tilde{\boldsymbol{\rho}}^{(z)} = \underset{\tilde{\boldsymbol{\rho}}^{(z)}\in S}{\arg\min} \left\| \tilde{\boldsymbol{\rho}}^{(z)} - \hat{\boldsymbol{\rho}}^{(z)} \right\|_2^2 \tag{50}$$

Step 5. Using $\tilde{\rho}^{(z)}$ simultaneously as the initialization for warm-start and as the proximal center, the subproblem (51) is computed by combining the global LCDR objective $J_L\left(\boldsymbol{E}^{(z)}, \boldsymbol{\rho}^{(z)}\right)$ in (45) with the proximal regularization term $\frac{\xi}{2}\|\boldsymbol{\rho}^{(z)} - \tilde{\boldsymbol{\rho}}^{(z)}\|_2^2$. Based on the solution $\boldsymbol{\rho}^{(z)}$, $EN_{n,t}^{(z)}$ is computed according to (45).

$$\begin{aligned} &\boldsymbol{\rho}^{(z)} = \underset{\boldsymbol{\rho}^{(z)}}{\arg\min} \left[J_L\left(\boldsymbol{E}^{(z)}, \boldsymbol{\rho}^{(z)}\right) + \frac{\xi}{2} \left\| \boldsymbol{\rho}^{(z)} - \tilde{\boldsymbol{\rho}}^{(z)} \right\|_2^2 \right] \\ &\text{s.t.}\, \boldsymbol{\rho}^{(z)} \in \mathcal{F}, \quad \left\| \boldsymbol{\rho}^{(z)} - \tilde{\boldsymbol{\rho}}^{(z)} \right\|_\infty \leq \Delta^{(z)} \end{aligned} \tag{51}$$

where $\Delta^{(z)}$ denotes the trust region.

Step 6. If $\|\boldsymbol{\rho}^{(z)} - \boldsymbol{\rho}^{(z-1)}\|_\infty \leq \varepsilon$, the iteration terminates and outputs the complete results of the source-side and load-side models; otherwise, set $z = z + 1$ and return $EN_{n,t}^{(z-1)}$ to **Step 4**.

The warm-start algorithm, as shown in Algorithm 1, constructs a mapping function based on the sample data of NCI and ECR to capture their relationship, thereby generating a candidate initialization. It further employs feasible-set projection to obtain refined initialization and adopts proximal regularization to enhance convergence stability. As a result, the number of source–load iterations is reduced, computational efficiency is significantly improved, and feasibility is guaranteed.

V. CASE STUDIES

The proposed methods are validated on an improved IEEE 39-bus system (Fig. 6), integrating an industrial load cluster of 15 EAF steel plants parameterized based on actual industrial data. The parameters of thermal power plants are listed in Table I. Time horizon T is 24 h, and τ is 15 min. This case represents a typical industry-dominated regional power system, where steel load accounts for the majority of total demand. This configuration highlights the role of the industrial cluster in coordinated source–load optimization. The detailed parameters and raw data for the case studies are available from the authors upon reasonable request.

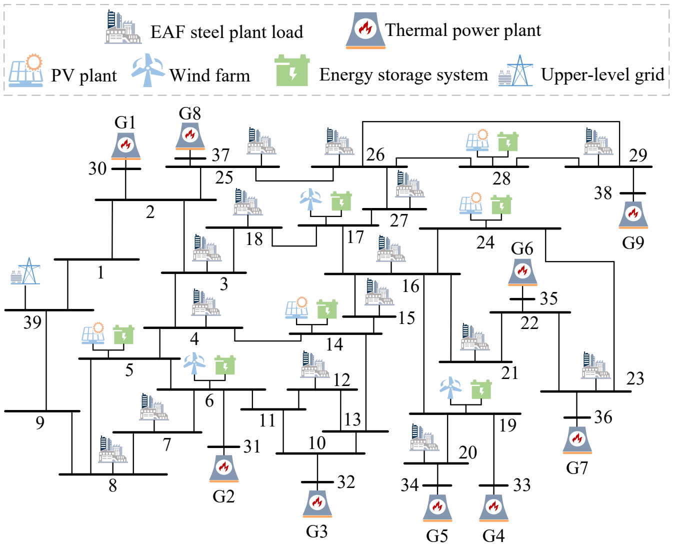

Fig. 6. System topology of the improved IEEE 39-bus system.

TABLE I
PARAMETER SETTINGS OF THERMAL POWER PLANTS

	Capacity (MW)	C_i^{G} (CNY/MWh)	C_i^{ON} (CNY/time)	C_i^{OFF} (CNY/time)	C_i^{MT} (CNY/time)	e_g (kgCO$_2$/MWh)
G1	800	510	43000	11000	54000	840
G2	740	570	40000	10000	50000	871
G3	870	490	47000	12000	59000	828
G4	740	570	40000	10000	50000	871
G5	540	690	29000	7000	36000	970
G6	770	540	42000	10500	52000	855
G7	640	640	34000	9000	43000	910
G8	600	670	32000	8000	40000	940
G9	900	440	48000	12500	61000	794

A. Analysis of Wasserstein-Based Source-Side DRO Model

To validate the effectiveness of the proposed DRO model, a series of historical sample sets of renewable energy are generated as shown in Table II. Several representative models are selected as benchmarks, including RO with a polyhedral uncertainty set (P-RO), moment-based DRO (M-DRO), Gaussian SP (GSP), and sample average approximation-based SP (SAA-SP). Default confidence level λ is set to 90%. N_{K} is measured in days.

Fig. 7 compares the operating costs of the representative models under different sample sizes. The operating costs of P-RO and GSP constitute the upper and lower bounds of all curves, respectively. This is because P-RO is independent of historical samples, whereas GSP assumes an explicit probability distribution derived from them. Therefore, P-RO and GSP yield the most conservative and aggressive decisions, respectively. M-DRO captures specific statistical features of historical data, utilizing the first-order moment to characterize the central tendency and the second-order moment to describe the variability of random variables. In this way, it achieves a certain degree of data-driven performance and reduces conservativeness compared with P-RO. However, since the moment-based ambiguity set does not converge to the true distribution even with increasing sample size, M-DRO fails to fully exploit larger sample sets to mitigate

TABLE II
Historical Sample Sets of Renewable Energy

Label	SA1	SA2	SA3	SA4	SA5	SA6
N_K	10	50	100	200	500	1000
Data points	6720	33600	67200	134400	336000	672000

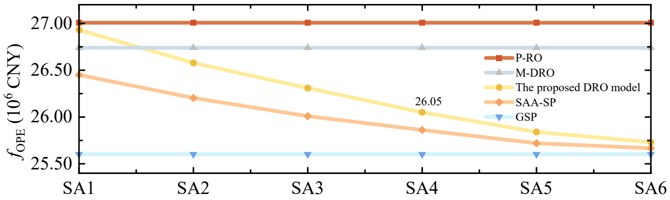

Fig. 7. Comparison of operating costs under different sample sizes.

decision conservativeness. Both the proposed DRO model and SAA-SP exhibit a decrease in operating cost as the sample size increases. This indicates that both models can leverage more samples to refine the estimation of probability distributions, thereby reducing decision conservativeness. To further evaluate the constraint feasibility of each model, we calculate the feasible levels of the constraints in Subsection C of Section III, and set 95% as the required minimum threshold for feasibility, as shown in Fig. 8(a). P-RO, M-DRO, and the proposed DRO model satisfy the required minimum threshold across all sample sets, demonstrating strong robustness. In contrast, GSP fails to meet the minimum threshold in any sample set due to its overly aggressive decisions. As the sample size increases, SAA-SP exhibits deteriorating constraint feasibility, failing to meet the minimum threshold in all sample sets beyond SA2. This indicates that, due to its aggressive decisions, SAA-SP exhibits poor constraint feasibility performance with larger sample sizes. In conclusion, the proposed DRO model strikes an optimal balance between robustness and feasibility. With sufficient data support, it yields superior economic performance, proving highly advantageous for source–load coordinated optimization.

Another notable advantage of the proposed DRO model is its two-stage deployment framework, consisting of an offline preparation stage and an operation stage. As illustrated in Fig. 8(b), the offline stage entails constructing the Wasserstein ambiguity set and reformulating the optimization model, facilitating flexible dataset maintenance and updates. Although the computation time of this stage increases moderately with the sample size, it remains acceptable as it is executed offline, imposing no impact on real-time dispatch. In contrast, the operation stage involves solving the reformulated optimization model. The computation time in this stage consistently remains below 25 s and shows no dependence on the sample size due to the sample-independent reformulation, which ensures its suitability for iterative source–load coordination. Consequently, the proposed framework leveraging offline data-driven preparation to enable computationally efficient real-time optimization.

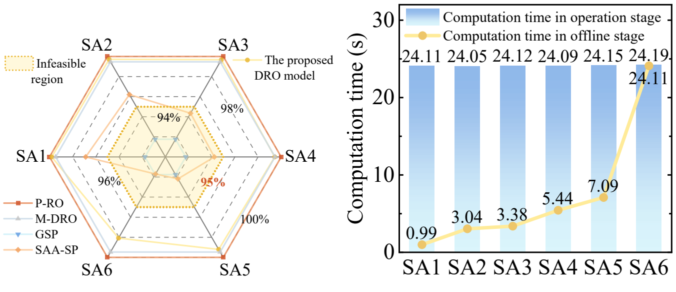

(a) (b)

Fig. 8. Constraint feasibility and computation time: (a) comparison of constraint feasibility with the required minimum threshold; (b) computation times in operation and offline stages.

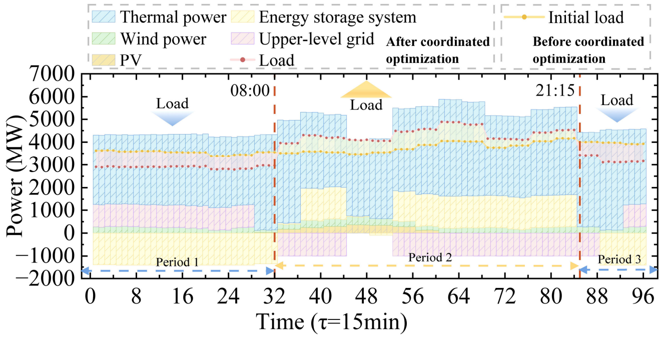

(a) Scenario 1

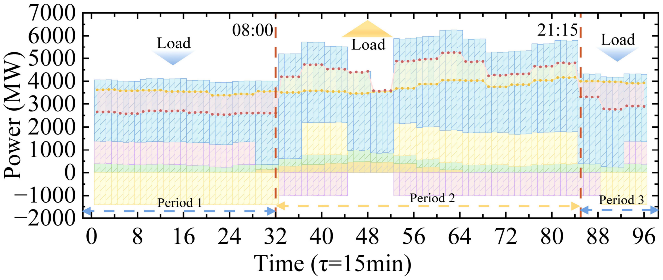

(b) Scenario 2

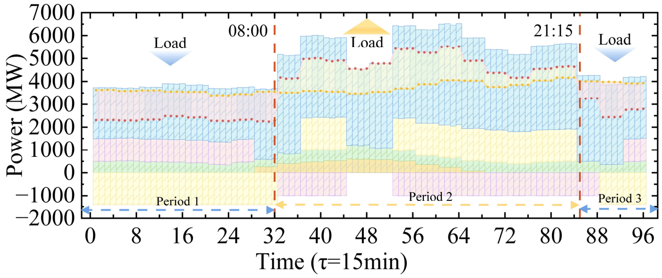

(c) Scenario 3

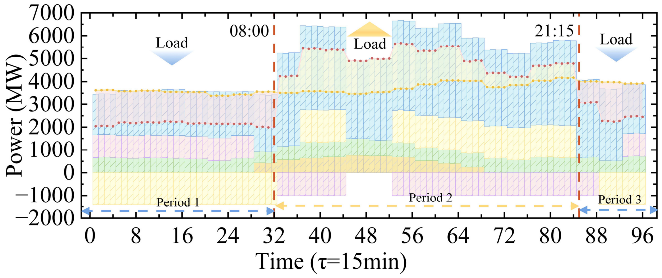

(d) Scenario 4

Fig. 9. Scheduling results of power sources and load adjustments.

B. Analysis of Source–Load Coordinated Optimization

To evaluate the effectiveness of the proposed source–load coordinated optimization method, four scenarios are defined according to different EECR levels, as shown in Table III. The historical sample set SA4 is selected for the source-side DRO model, since SA4 not only provides sufficient data support but also ensures that the constraint feasibility of the DRO model remains close to 100%.

The scheduling results of power sources from the source-side

TABLE III
SCENARIO CLASSIFICATION UNDER DIFFERENT EECR LEVELS

Label	Scenario 1	Scenario 2	Scenario 3	Scenario 4
$\rho^{\max}$	4%	6%	8%	10%

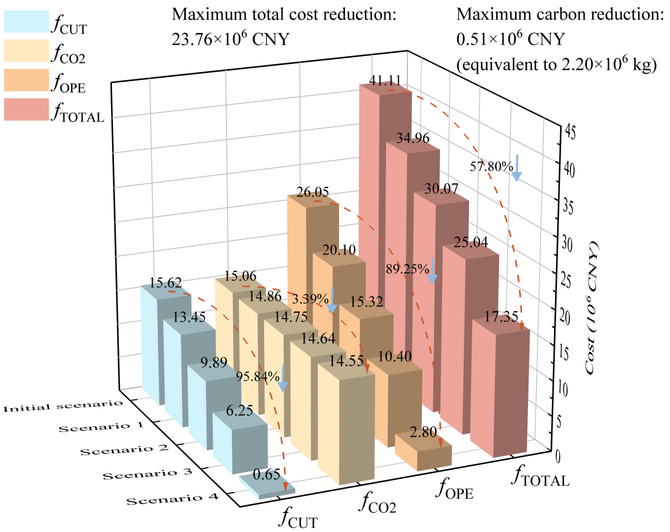

Fig. 10. Costs of the system under different scenarios.

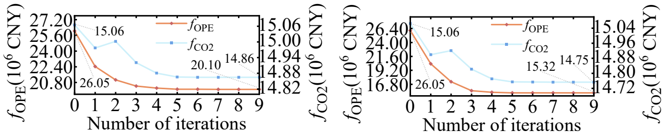

(a) Scenario 1 (b) Scenario 2

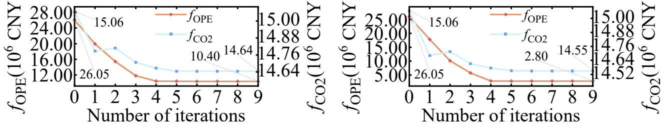

(c) Scenario 3 (d) Scenario 4

Fig. 11. Iterative processes under different scenarios.

DRO model and the load adjustments from the load-side LCDR model under the four scenarios are compared in Fig. 9(a)–(d). From the perspective of power sources, as the adjustment capability of EAF steel plant cluster participating in LCDR increases (with $\rho^{\max}$ gradually increasing from Scenario 1 to Scenario 4), the output of thermal generation gradually decreases. Meanwhile, the utilization of wind and PV resources significantly improves. These results demonstrate that the proposed method, through source–load coordinated optimization, enhances the flexibility of power sources, reduces the operational burden on thermal generation, and facilitates renewable energy integration. From the load perspective, during 00:00–08:00 (Period 1) and 21:15–24:00 (Period 3), the overall load demand decreases (red-shaded regions), whereas during 08:00–21:15 (Period 2), the demand increases (yellow-shaded region). This trend becomes more pronounced as $\rho^{\max}$ increases, indicating that the load-side adjustment capacity expands with the release of EAF steel plant cluster participating in LCDR. The proposed method effectively exploits the demand-side flexibility of the EAF steel plant cluster, enabling more production tasks to be shifted from periods with insufficient renewable generation (Periods 1 and 3) to the period with higher renewable output (Period 2), thereby achieving a higher share of low-carbon production. Meanwhile, the load adjustment exhibits an overall "smooth-shifting" pattern rather than frequent on/off fluctuations. This demonstrates that the proposed method leverages demand-side flexibility while strictly adhering to the process constraints of EAF steelmaking, such as batch processing. In other words, the EAF steelmaking process can be reasonably rescheduled within allowable time windows but cannot be arbitrarily interrupted, ensuring the feasibility of industrial production scheduling. In addition, from the perspective of production tasks, the unchanged total energy consumption (with the areas of the two red-shaded regions equal to that of the yellow-shaded region) indicates that the proposed method also ensures sufficient energy supply for the EAF steel plant cluster within time horizon T.

To further verify that the proposed method enables low-carbon economic operation of the system, the costs under different scenarios are presented in Fig. 10. The total system cost f_{TOTAL} is defined as the sum of the operating cost f_{OPE} and the carbon emission cost f_{CO2}. An initial scenario is defined in which neither source–load model iteration nor LCDR is performed. Instead, the carbon emission cost is calculated directly through NCI and initial energy consumption, such that the initial scenario degenerates into the proposed DRO model performing only economic optimization of the system. From Fig. 10, as the adjustment capability of load-side EAF steel plant cluster increases, the total system cost decreases by 23.76×10^6 CNY, representing a reduction of 57.80%. This reduction is mainly attributed to the operating cost, which drops from 26.05×10^6 CNY to 2.80×10^6 CNY, yielding a decline of 89.25%. In particular, the cost of renewable energy curtailment, a non-negligible component of the operating cost, falls by 14.97×10^6 CNY, with a reduction exceeding 95%. Meanwhile, this still results in a maximum reduction of 2.20×10^6 kg in carbon emissions. These results demonstrate that the proposed method alleviates renewable energy curtailment and reduces carbon emissions. It achieves cost savings through enhanced integration of zero-carbon power sources and carbon reduction incentives. In this way, the system can achieve low-carbon economic operation. Moreover, as the share of the EAF steel plant cluster participating in LCDR increases, the cost-saving benefits become more pronounced, further confirming the effectiveness of the proposed method under scenarios with larger steel loads engaged in LCDR. The iterative processes under different scenarios shown in Fig. 11 indicate that even with an increasing share of the EAF steel plant cluster participating in LCDR, the proposed method can still achieve stable convergence within a limited number of iterations, demonstrating its robustness.

From the modeling perspective, the proposed method achieves lower costs across all categories compared with initial scenario. The results of Fig. 11 demonstrate that multiple iterations of source–load coordinated optimization can fully activate the interactive potential of both supply-side and demand-side resources. By enabling bidirectional dynamic decision-making rather than one-sided, one-shot decisions, the method further reduces the conservativeness of the proposed DRO model.

C. Analysis of Warm-Start Based Source–Load Coordinated Optimization Algorithm

By selecting Scenario 4, which specifies the largest $\rho^{\max}$, Fig. 12(a) presents the sample data of NCI and ECR for the entire

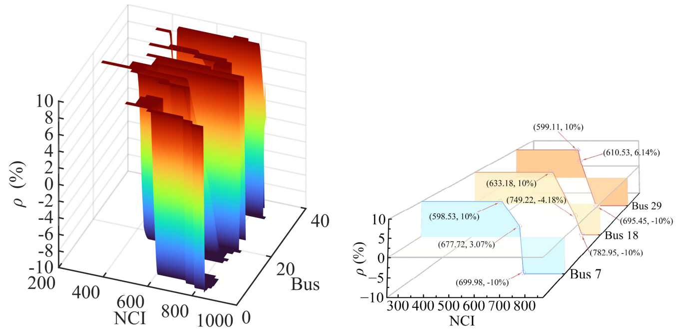

(a) (b)

Fig. 12. Data-driven construction of mapping functions: (a) sample data of NCI and ECR under Scenario 4; (b) mapping functions for buses 7, 18, and 29 under Scenario 4.

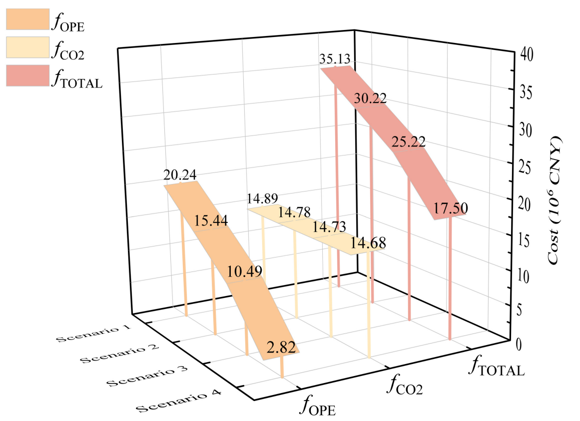

(a) Objective functions under different scenarios

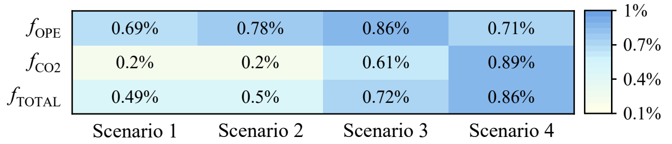

	Scenario 1	Scenario 2	Scenario 3	Scenario 4
f_{OPE}	0.69%	0.78%	0.86%	0.71%
f_{CO2}	0.2%	0.2%	0.61%	0.89%
f_{TOTAL}	0.49%	0.5%	0.72%	0.86%

(b) Relative deviations between the proposed source–load coordinated optimization method and its warm-start algorithm

Fig. 13. Analysis of the proposed warm-start algorithm from the optimization perspective.

system, and Fig. 12(b) illustrates the mapping functions for buses 7, 18, and 29. The mapping functions in Fig. 12(b) reflect the willingness of the EAF steel plant at the corresponding bus to participate in LCDR under different NCI levels. A positive ρ indicates an intention to increase energy consumption, whereas a negative ρ indicates an intention to decrease energy consumption. Taking bus 7 as an example, the mapping function and its inflection points indicate the following. When the NCI ranges from 0 to 598.53 kgCO$_2$/MWh, the EAF steel plant shows the highest positive willingness to consume electricity, implying that the associated carbon emissions are relatively low. When the NCI falls within 598.53–699.98 kgCO$_2$/MWh, the willingness gradually decreases. Once the NCI exceeds 699.98 kgCO$_2$/MWh, the EAF steel plant becomes least willing to consume electricity, suggesting that the carbon emissions are excessively high and the plant aims to shift energy consumption to the maximum extent possible. The mapping functions provide support for generating candidate initialization.

To verify the effectiveness from the optimization perspective, the objective functions obtained by the proposed warm-start algorithm under different scenarios are presented in Fig. 13(a). Furthermore, the relative deviations between the objective functions obtained by the proposed warm-start algorithm and those from the source–load coordinated optimization method are shown in Fig. 13(b). To validate the computational efficiency of the proposed algorithm, the initial scenario, the proposed warm-start algorithm, and the proposed source–load coordinated optimization method are denoted as Method I, Method II, and Method III, respectively. The computation times under different scenarios are compared in Fig. 14, while the numbers of iterations under different scenarios are presented in Fig. 15.

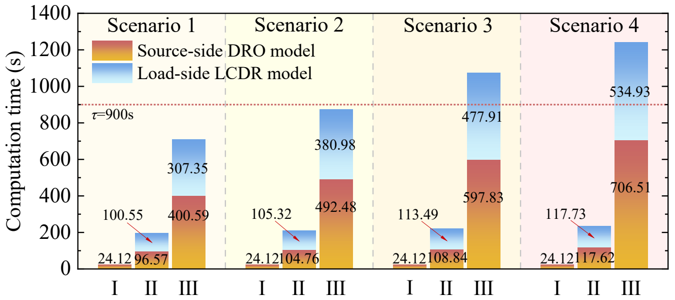

Fig. 14. Comparison of computation times under different scenarios.

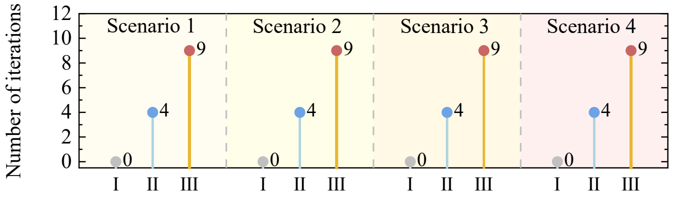

Fig. 15. Comparison of numbers of iterations under different scenarios.

From Fig. 14, it can be observed that as the adjustment capability of the EAF steel plant cluster increases, the total computation time of Method I remains unchanged. In contrast, the total computation time of Method II increases from 197.12s to 235.35s, while that of Method III increases from 707.94s to 1241.44s. By combining the results in Figs. 14 and 15, several analytical conclusions can be drawn. Method I exhibits the shortest computation time since it does not involve source–load coordination and LCDR. Method III shows the longest computation time, because the increasing adjustment capability of the EAF steel plant cluster intensifies oscillations of the decision variables (i.e., adjusted load profiles). The oscillations and iterations form a vicious cycle, which continuously amplifies their adverse effects and progressively increases the computational burden of both the source-side and load-side models. As a result, nine iterations are required for decision variables of all buses to converge, and the total computation time exceeds the unit time slot τ, imposing practical limitations. Method II, equipped with warm-start and proximal regularization for oscillation suppression, avoids excessive iterations. Consequently, it achieves a relatively short and stable computation time, which is almost unaffected by the increase in adjustment capability.

Considering both optimization performance and computation time, an analysis of the results in Figs. 10, 13, 14, and 15 is conducted. Method I yields the shortest computation time. However, it does not exploit any source–load interaction, leading to the highest operating cost, carbon emission cost, and total cost. Hence, it cannot provide a low-carbon and economic decision.

Method III fully coordinates source-side and load-side resources to achieve a balanced decision and delivers the most economic results. Nevertheless, as the load of the EAF steel plant cluster participating in LCDR increases, the total computation time becomes uncontrollable, rendering it unsuitable for both power source scheduling and steel production scheduling. Method II retains the advantages of Method III in enabling low-carbon economic operation. It enhances source-side resilience against renewable fluctuations and encourages participation of the EAF steel plant cluster in LCDR. Compared with Method III, Method II improves computation efficiency significantly, while the loss in economic performance remains below 1%. Most importantly, Method II prevents excessive iterations and keeps the total computation time stably within a reasonable range.

VI. Conclusion

This paper proposes a source–load coordinated optimization method considering the participation of EAF steel plant cluster in LCDR. By accommodating the specific production constraints of EAF steelmaking, the proposed method enables the smooth shifting of industrial loads to periods of high renewable generation, significantly facilitating renewable energy integration. Numerical results show that, compared with conventional methods, the proposed method reduces carbon emissions by up to 2.20×10^6 kg, decreases the cost of renewable energy curtailment by 14.97×10^6 CNY, and lowers the total system cost by 57.80%. Moreover, both carbon reduction and cost-saving performance are further enhanced as the adjustment capacity of the EAF steel plant cluster increases. To address the issue of excessive iteration time in the source–load models, the proposed warm-start algorithm limits the total computation time to within 240s, with less than 1% loss in economic performance, thereby achieving fast optimization within a unit time slot. The proposed method enables low-carbon economic operation of power systems considering the regulation of EAF steel plant cluster, thereby providing a new perspective for future power system decarbonization in industrial scenarios.

References

[1] J. Wessel, A. K. Chowdhury, T. Wild, F. Kanyako, G. Iyer, and J. Lamontagne, “Regional coordination can alleviate the cost burden of a low-carbon electricity system,” *Nature Communications*, vol. 16, no. 1, p. 9033, 2025.

[2] X. Gao, S. Wang, Y. Sun, J. Zhai, N. Chen, and X.-P. Zhang, “Low-carbon energy scheduling for integrated energy systems considering offshore wind power hydrogen production and dynamic hydrogen doping strategy,” *Applied Energy*, vol. 376, p. 124194, 2024.

[3] L. Yao, Y. Wang, and X. Xiao, “Concentrated solar power plant modeling for power system studies,” *IEEE Transactions on Power Systems*, vol. 39, no. 2, pp. 4252–4263, 2023.

[4] V. Vogl, O. Olsson, and B. Nykvist, “Phasing out the blast furnace to meet global climate targets,” *Joule*, vol. 5, no. 10, pp. 2646–2662, 2021.

[5] World Steel Association, “World steel in figures 2025,” [Online]. Available: https://worldsteel.org/data/world-steel-in-figures/world-steel-in-figures-2025/, 2023, accessed: Oct. 18, 2025.

[6] B. K. Sovacool, F. W. Geels, and M. Iskandarova, “Industrial clusters for deep decarbonization,” *Science*, vol. 378, no. 6620, pp. 601–604, 2022.

[7] C. Schneider, “Steel manufacturing clusters in a hydrogen economy–simulation of changes in location and vertical integration of steel production in northwestern europe,” *Journal of Cleaner Production*, vol. 341, p. 130913, 2022.

[8] X. Dong, C. Jiang, J. Liu, D. Zhao, and B. Sun, “Model predictive control optimization strategy for integrated energy systems: A two-stage dual-loop optimization framework,” *IEEE Transactions on Sustainable Energy*, vol. 15, no. 4, pp. 2234–2248, 2024.

[9] M. Song, Z. Xu, C. Gao, M. Yan, and Q. Hu, “Distribution dynamic operating security space characterization for aggregation and congestion capacity evaluation of virtual power plant,” *IEEE Transactions on Smart Grid*, 2025.

[10] J. Ruan, G. Liu, J. Qiu, G. Liang, J. Zhao, B. He, and F. Wen, “Time-varying price elasticity of demand estimation for demand-side smart dynamic pricing,” *Applied Energy*, vol. 322, p. 119520, 2022.

[11] Y. Li, N. Zhang, E. Du, Y. Liu, X. Cai, D. He *et al.*, “Mechanism study and benefit analysis on power system low carbon demand response based on carbon emission flow,” *Proc. CSEE*, vol. 42, no. 08, pp. 2830–2842, 2022.

[12] C. Li, Z. Yan, Y. Yao, Y. Deng, C. Shao, and Q. Zhang, “Coordinated low-carbon dispatching on source-demand side for integrated electricity-gas system based on integrated demand response exchange,” *IEEE Transactions on Power Systems*, vol. 39, no. 1, pp. 1287–1303, 2023.

[13] Y. Zhang, P. Sun, X. Ji, M. Yang, and P. Ye, “Low-carbon economic dispatch of integrated energy systems considering full-process carbon emission tracking and low carbon demand response,” *IEEE Transactions on Network Science and Engineering*, vol. 11, no. 6, pp. 5417–5431, 2024.

[14] H. Gao, B. Yin, S. He, and J. Liu, “A distributionally robust-based information gap decision theory optimization method for energy station considering low-carbon demand response,” *Sustainable Energy Technologies and Assessments*, vol. 73, p. 104129, 2025.

[15] Q. Ge, C. Guo, H. Jiang, Z. Lu, G. Yao, J. Zhang, and Q. Hua, “Industrial power load forecasting method based on reinforcement learning and pso-lssvm,” *IEEE transactions on cybernetics*, vol. 52, no. 2, pp. 1112–1124, 2020.

[16] S. S. Foslie, J. Straus, B. R. Knudsen, and M. Korpås, “Decarbonizing integrated chlor-alkali and vinyl chloride monomer production: Reducing the cost with industrial flexibility,” *Advances in Applied Energy*, vol. 12, p. 100152, 2023.

[17] Y.-Q. Bao, X.-R. Song, and P.-C. Zhou, “Stackelberg-game-based energy optimization strategy for interactive energy use of flexible manufacturing industrial parks,” *Applied Energy*, vol. 401, p. 126701, 2025.

[18] N. Zhang, L. Du-Ikonen, X. Lin, W. Zhong, M. Ropo, and L. Jiang, “Co-ordinated scheduling and carbon flow tracing of discrete manufacturing processes with integrated energy-material-carbon flows model,” *Applied Energy*, vol. 398, p. 126435, 2025.

[19] Y. Yang, J. C.-H. Peng, and Z.-S. Ye, “Distributionally robust frequency dynamic constrained unit commitment considering uncertain demand-side resources,” *Applied Energy*, vol. 331, p. 120392, 2023.

[20] J. Zhai, Y. Jiang, M. Zhou, Y. Shi, W. Chen, and C. N. Jones, “Data-driven joint distributionally robust chance-constrained operation for multiple integrated electricity and heating systems,” *IEEE Transactions on Sustainable Energy*, vol. 15, no. 3, pp. 1782–1798, 2024.

[21] L. Zhang, K. Zhang, Z. Zheng, Y. Chai, X. Lian, K. Zhang, Z. Xu, and S. Chen, “Two-stage distributionally robust integrated scheduling of oxygen distribution and steelmaking-continuous casting in steel enterprises,” *Applied Energy*, vol. 351, p. 121788, 2023.

[22] C. Ning, A. Ma, and Z. Dong, “Data-driven multi-stage distributionally robust scheduling for coupled electricity-hydrogen-refinery systems,” *Applied Energy*, vol. 401, p. 126620, 2025.

[23] L. Fu, H. Chen, R. Zhang, T. Jiang, G. Li, and R. Qu, “Distributionally robust chance-constrained energy management of steel industrial microgrid with energy storage in distribution market,” *Applied Energy*, vol. 400, p. 126574, 2025.

[24] X. Zhang, G. Hug, and I. Harjunkoski, “Cost-effective scheduling of steel plants with flexible eafs,” *IEEE Transactions on Smart Grid*, vol. 8, no. 1, pp. 239–249, 2016.

[25] R. Lyu, X. Su, E. Du, H. Guo, Q. Chen, and C. Kang, “Efficient scheduling of discrete industrial processes through continuous modeling,” *IEEE Transactions on Smart Grid*, 2025.

[26] Y. Cheng, N. Zhang, Y. Wang, J. Yang, C. Kang, and Q. Xia, “Modeling carbon emission flow in multiple energy systems,” *IEEE Transactions on Smart Grid*, vol. 10, no. 4, pp. 3562–3574, 2018.

[27] Z. Fan and S. J. Friedmann, “Low-carbon production of iron and steel: Technology options, economic assessment, and policy,” *Joule*, vol. 5, no. 4, pp. 829–862, 2021.

[28] C. Duan, W. Fang, L. Jiang, L. Yao, and J. Liu, “Distributionally robust chance-constrained approximate ac-opf with wasserstein metric,” *IEEE Transactions on Power Systems*, vol. 33, no. 5, pp. 4924–4936, 2018.

[29] R. Zhu, H. Wei, and X. Bai, “Wasserstein metric based distributionally robust approximate framework for unit commitment,” *IEEE Transactions on Power Systems*, vol. 34, no. 4, pp. 2991–3001, 2019.